JGR Atmospheres

RESEARCH ARTICLE
10.1029/2020JD033610

Sensitivity of Air-Sea Heat Exchange in Cold-Air Outbreaks to Model Resolution and Sea-Ice Distribution

C. Spensberger[1] and **T. Spengler**[1]

[1]Geophysical Institute, University of Bergen, and Bjerknes Centre for Climate Research, Bergen, Norway

Key Points:

- Evaporation and precipitation increase in tandem with increasing resolution
- Sharper resolved marginal ice zones yield higher peak and overall heat uptake
- Overall sensible heat uptake and moisture balance is consistent across resolutions

Supporting Information:

- Figure S1

Correspondence to:
C. Spensberger,
clemens.spensberger@uib.no

Citation:
Spensberger, C., & Spengler, T. (2021). Sensitivity of air-sea heat exchange in cold-air outbreaks to model resolution and sea-ice distribution. *Journal of Geophysical Research: Atmospheres*, *126*, e2020JD033610. https://doi.org/10.1029/2020JD033610

Received 8 SEP 2020
Accepted 12 JAN 2021

Author Contributions:
Formal analysis: C. Spensberger
Methodology: C. Spensberger, T. Spengler
Visualization: C. Spensberger
Writing – original draft: C. Spensberger, T. Spengler
Writing – review & editing: C. Spensberger, T. Spengler

Abstract Modeling air-sea interactions during cold air outbreaks poses a major challenge because of the vast range of scales and physical processes involved. Using the Polar WRF model, we investigate the sensitivity of downstream air mass properties to (a) model resolution, (b) the sharpness of the marginal-ice zone (MIZ), and (c) the geometry of the sea ice edge. The resolved sharpness of the MIZ strongly affects peak heat fluxes and the atmospheric water cycle. For sharper MIZs, roll convection is initiated closer to the sea ice edge, increasing both evaporation and precipitation. This yields an increased heat transfer into the atmosphere while the net effect on the atmospheric moisture budget is small. Overall, higher atmospheric resolution increases both the peak and net heat extracted from the ocean. The geometry of the sea ice edge can induce convergence or divergence zones that affect the air-sea exchange.

Plain Language Summary In the Arctic, sea-ice insulates a relatively warm ocean from a rather cold atmosphere. From time to time, very cold air masses spill out from the sea ice over the open ocean. When this happens, large amounts of heat and moisture are released from the ocean into the atmosphere, heating and moistening the air above while cooling the ocean. In this study, we investigate how the modeled heat and moisture exchange depends on the resolution of the atmospheric model and on properties of the marginal ice zone between the pack ice and the open ocean. The higher the resolution of the atmospheric model and the sharper the transition from the pack ice to the open ocean, the more heat and moisture is released from the ocean into the atmosphere. This dependence of the heating on model resolution is particularly pronounced close to the sea-ice edge.

1. Introduction

Marine cold air outbreaks (CAOs) constitute a large fraction of the air-sea heat exchange in the polar regions (e.g., Papritz & Spengler, 2017). These atmosphere-ocean interactions are most intense near the sea ice edge and within the Marginal Ice Zone (MIZ), which is also the location where our models and are often least accurate (e.g., Bourassa et al., 2013, 2021). In addition to challenges with parameterizations, the magnitude and distribution of these air-sea heat exchanges are also sensitive to the representation of mesoscale atmospheric phenomena (e.g., Condron et al., 2008; Condron & Renfrew, 2013; Isachsen et al., 2013), the sea ice distribution (Seo & Yang, 2013; Renfrew et al., 2021), and model resolution (e.g., Haarsma et al., 2016; Jung et al., 2014; Moore et al., 2016). To map these sensitivities, we perform a suite of idealized CAO simulations where we vary the model resolution as well as the sea ice concentration within the MIZ.

The MIZ exhibits strong trends in position and width in association with the warming Arctic (Strong, 2012). In this context, our suite of idealized CAO simulations will help to better understand the implications of the warming Arctic for air-sea heat exchange and shed light on potential origins of biases in climate models. For example, changes in sea ice distribution have already been linked to significant changes in the air-sea heat exchange and associated impact on convection in the ocean (Vage et al., 2018). The area around the MIZ is thus of great importance for these exchange mechanisms and feedbacks between the atmosphere, sea ice, and the ocean (Spengler et al., 2016), where the representation of these mechanisms and their intensity can be dependent on model resolution and sea ice distribution.

As models with a resolution typical to global climate models generally fail to reproduce mesoscale atmospheric features and seriously underestimate wind intensity (e.g., Moore et al., 2016), it is important to understand the impact of model resolution on atmosphere-ocean heat exchange. With oceanic convection often driven by episodic strong wind events and CAOs (e.g., Pickart et al., 2003; Renfrew et al., 2019; Vage

et al., 2008), investigating these resolution dependencies will also shed light on potential impacts on deep water formation. In the North Atlantic, this formation of dense water is essential for feeding the meridional overturning circulation (e.g., Dickson et al., 1996; Gebbie & Huybers, 2010). It has been shown that a higher atmospheric resolution can lead to either a 5%–10% increase in the strength of the Atlantic meridional overturning circulation (AMOC) in an ocean only simulation (Jung et al., 2014) or to a weaker AMOC in fully coupled climate models (Sein et al., 2018). This controversy asks for a more detailed understanding of the resolution dependence of the pertinent processes associated with these air-sea interactions. As a step in this direction, we here use idealized atmosphere-only simulations to systematically assess the representation of the air-sea heat exchange in CAOs across different model resolutions.

In addition, CAOs can be conducive to extreme weather events such as polar lows and polar mesoscale cyclones (e.g., Michel et al., 2018; Stoll et al., 2018; Stoll et al., 2021; Terpstra et al., 2016). Some of these cyclones can also experience explosive growth leading to extreme latent and sensible heat as well as momentum fluxes (e.g., Inoue & Hori, 2011). Exploring the sensitivity of the evolution of CAOs and their associated air-sea heat exchange with respect to model resolution and sea ice distribution in the MIZ will thus also yield insights into the minimum requirements to adequately predict the essential ingredients giving rise to these phenomena. With the increasing availability of computational resources, model simulations often employ increasingly higher resolutions. How to make the most optimal use of the available resources with respect to model resolution to resolve the pertinent processes, however, remains an open question. Similar to Sein et al. (2018), we thus explore the gain and loss with respect to changes in spatial resolution for the representation of air-sea heat exchange in CAOs in an atmosphere-only setup.

2. Model Setup

We base our analysis on a series of idealized model simulations using Polar WRF version 3.9.1 (Hines et al., 2015). We analyze an inner domain of 3,072 × 3,072 km with a grid spacing of either 3, 6, 12, 24, 48, or 96 km. This corresponds to a size of the inner domain between 1,024 × 1,024 and 32 × 32 grid points. For all horizontal resolutions, the vertical grid encompasses 60 hybrid model levels with a grid spacing of about 8–10 hPa in the lowest 3 levels and about 25 hPa in the mid-troposphere.

We initialize the domain with horizontally homogeneous winds blowing across an ice edge toward the open ocean. The inital winds are balanced using the method of (Terpstra & Spengler, 2015). Near-surface wind speeds are initialized with 20 m/s (Figure 1a), but equilibrate to approximately 12–13 m/s over sea ice and 15–16 m/s over open water due to boundary layer processes. These wind speeds are on the upper end of the wind speeds observed during the ARKTIS1993 campaign (Brummer, 1996, 1997). We repeated the control simulation with initialized winds reduced to 10 m/s, which does not qualitatively change our results. In particular, the dependence of the results on model resolution remains unchanged.

We prescribe a stable temperature profile with 255 K near-surface temperatures and a constant stratification equivalent to a buoyancy oscillation frequency $N^2 = 2.25 \cdot 10^{-4}\ s^{-2}$ (Figure 1b). Above the tropopause at 6 km height, stratification increases to $N^2 = 4.0 \cdot 10^{-4}\ s^{-2}$ (Figure 1b). These initial values are prescribed along all lateral boundaries throughout the simulation.

To avoid contamination of the inner domain by the boundary forcing, we pad the inner domain by 8 grid points along all lateral boundaries, resulting in a size of the full domain between 1,040 × 1,040 and 48 × 48 grid points (inner domain: thick gray box, full domain: black box in Figure 1c). WRF nudges toward the prescribed boundary values in the outermost 5 grid points of the model domain.

In the control setup, we place a straight sharp sea ice edge 480 km downstream of the inflow boundary of the inner domain (pale red rectangle in Figure 1c). Upstream of the sea ice edge we set the ice concentration to 100%, and skin temperatures to 255 K. Over open water, we set the skin temperature to freezing conditions for typical salt water, 271.3 K. We tested the sensitivity of our results to the choice of the SST distribution with two experiments, (a) by uniformly increasing SSTs to 278 K, and (b) by linearly increasing SSTs from the freezing point at the sea-ice edge by 8 K per 1,000 km downstream distance. This SST gradient corresponds to the mean SST increase across the Nordic Seas from the Greenland East coast to Northern Norway.

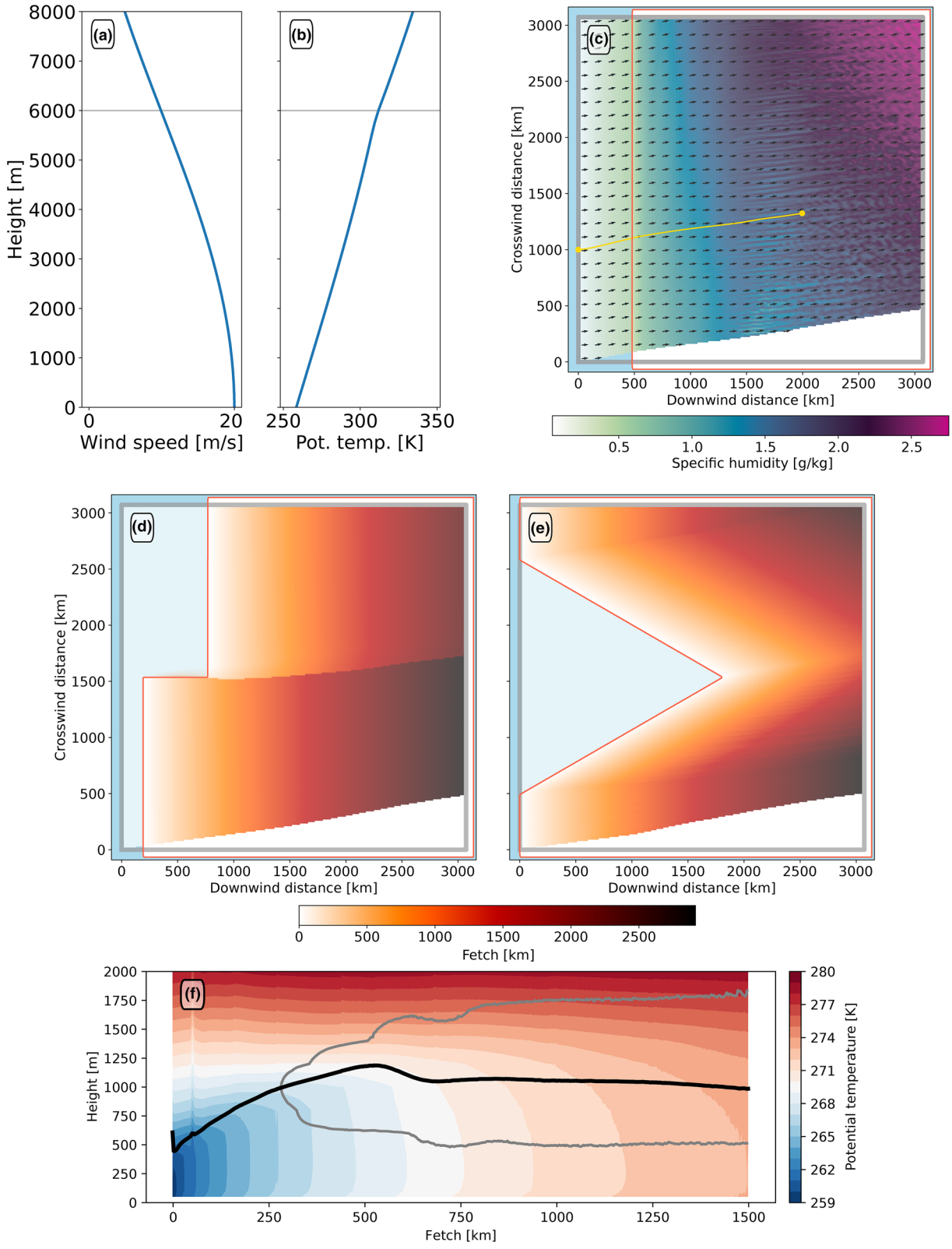
(a)
(b)
(c)
(d)
(e)
(f)
Height [m]
Wind speed [m/s]
Pot. temp. [K]
Crosswind distance [km]
Downwind distance [km]
Specific humidity [g/kg]
Fetch [km]
Potential temperature [K]

In both sensitivity experiments, local fluxes increase in tandem with the increasing air-sea temperature contrast, but the dynamics of the CAO and dependence on atmospheric resolution remain unchanged.

Along all boundaries we prescribe the initial and inflow conditions throughout the model simulation. As these conditions represent a stable atmospheric column over sea ice, we linearly increase the sea-ice concentration from open water to full sea ice cover along the outermost 5 grid points of the full domain (pale red contour in Figure 1c). This linear increase is consistent with WRF nudging the outermost 5 grid points to the prescribed boundary values.

We follow the configuration of the Antarctic Mesoscale Prediction System (AMPS, Manning, 2019), except for the boundary layer parameterization. In our tests the AMPS parameterization produced unphysical discontinuities in boundary layer properties, possibly related to changes in the diagnosed boundary layer regime (see supplement for details). We find similar discontinuities with the QNSE scheme (Sukoriansky et al., 2005), but not with the YSU-scheme (Hong et al., 2006) and the MYNN2.5 and MYNN3 schemes (Nakanishi & Niino, 2006, 2009). As YSU is the default for standard WRF 3.9.1, we decided to use the YSU scheme for our simulations. The MYNN2.5 and MYNN3 schemes yield qualitatively similar results to the YSU scheme (comparison for control setup in supplement).

Besides the boundary layer parametrization, we use the Kain-Fritsch cumulus parametrization for simulations with a grid spacing greater and equal to 12 km (Kain, 2004). At all resolutions, we use the Purdue-Lin microphysics scheme with ice, snow, and graupel processes (Chen & Sun, 2002). We disable radiation and keep skin temperatures constant throughout the simulation. There is thus no diurnal cycle in the surface energy budget, and no longwave radiative cloud feedback. While radiation likely plays an important role in real-world cold-air outbreaks, the success of very idealized models (like the mixed layer model of Renfrew & King, 2000) demonstrates that qualitatively realistic CAOs can be simulated without radiative feedbacks.

We integrate the model for 96 h. The simulated fluxes reach a statistical equilibrium throughout the inner domain by 48 h of integration. As flow at 20 m/s travels for about 3,500 km in 48 h, the numerical shock associated with slight imbalances in the initial conditions has traveled out of the domain at this point in time. We thus use the final 48 h of each simulation for our analysis.

3. Comparing Simulations Based on Fetch

We analyze surface fluxes, precipitation and boundary layer properties as a function of fetch d,

$$d(s) = \int_{s=0}^{s} \big(1 - c(s)\big) ds, \tag{1}$$

the distance traveled over open water. In this equation, $c(s)$ is the local sea ice concentration varying between 1 and 0 and s is the distance along a streamline (yellow line in Figure 1c as example), with $s = 0$ at the inflow boundary of the inner domain. Upstream of this inflow boundary, sea ice concentration is kept at 100% for all simulations.

We determine the fetch based on the horizontal time-average flow during the analysis period (48–96 h) at 300 m above sea level. Using the time-average flow, we calculate streamlines backward from every grid point to trace the flow to the inflow boundary of the inner domain ($x = 0$ in Figure 1c). Grid points where the streamlines do not trace back to the inflow boundary are discarded. For the control setup, this is the case for all grid points in the white wedge in the lower right corner of the inner domain (Figure 1c).

Figure 1. (a, b) Vertical profiles of wind speed and potential temperature used at the initial time and at the upstream boundary around the cross-wind center of the domain. (c) Specific humidity (g/kg) (semi-transparent shading) at 90 h together with wind (arrows) at 300 m above ground level. The yellow line exemplifies a streamline used for the fetch calculation. The pale red contour in (c–e) marks the 50% sea ice concentration, with ice-covered areas marked by a pale blue background. The gray frames in (c–e) indicate the inner domain used for the analyses. Grid points unreachable by horizontal advection from the inflow boundary appear white and are disregarded in the fetch-based analyses. The semi-transparent shading in (d, e) shows fetch [km] for a simulation (d) with a step in the sea ice edge, and (e) a triangular ice edge, both with with 12 km grid spacing. The simulations are referred to as S576 and Δ60, respectively, in Section 7. (f) Average evolution of potential temperature [K] (shading), boundary layer height (black line), and extent of the cloud layer (gray contour) as a function of fetch for all streamlines in the control simulation with 3 km grid spacing.

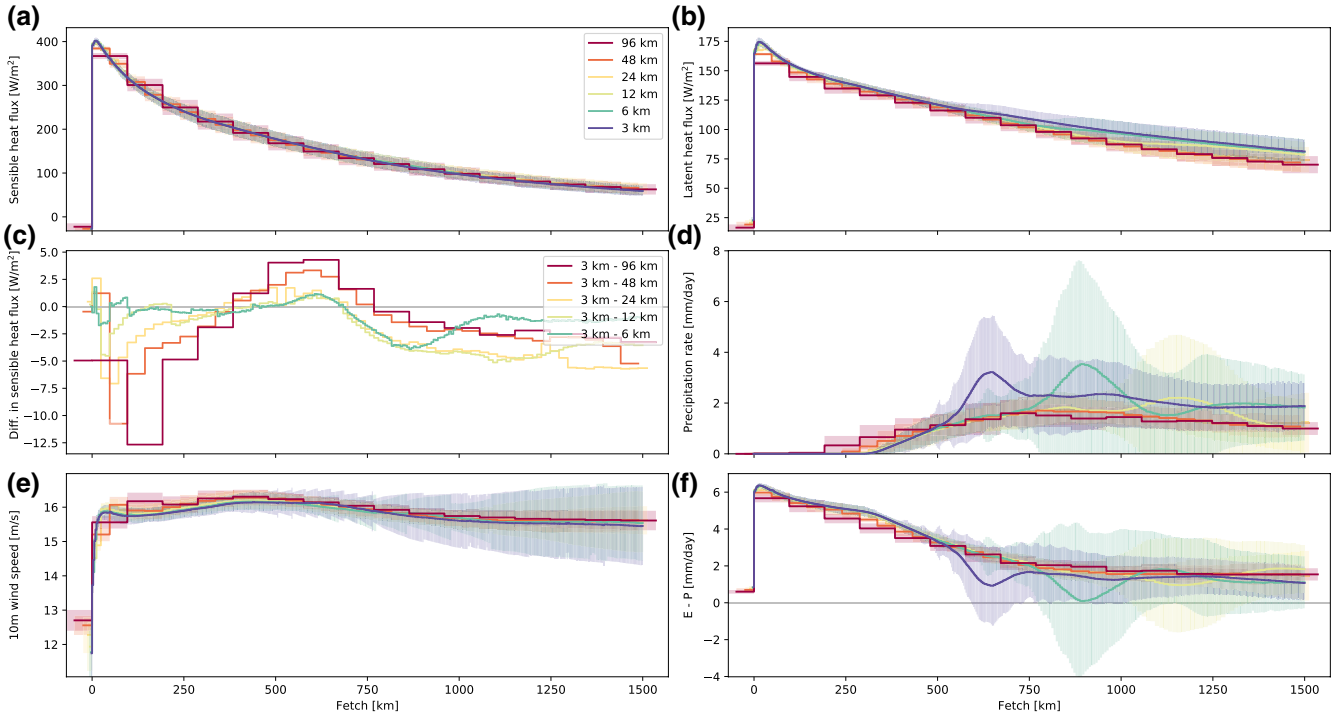

Figure 2. Evolution of the simulated air-sea interaction with fetch. The panels show (a) sensible heat flux (b) latent heat flux, (c) difference in sensible heat flux between resolutions, (d) precipitation rate, (e) 10-m wind speed U_{10}, and (f) evaporation minus precipitation ($E - P$). To calculate the differences in (c), the 3 km-simulation has been interpolated to the respective lower resolution. Transparent shading around lines indicates the standard deviation among all points with the same fetch. Line colors are consistent throughout the panels, except for the difference plot (c).

Two example fetch calculations in Figures 1d and 1e illustrate the procedure. For a step in the ice edge, the fetch calculation yields a well-defined discontinuity along the convergence zone emerging from the step (Figure 1d). Further, a slight on-ice flow component across the downwind oriented section of the sea ice edge yields slightly positive fetch values for the first grid points over the sea ice (Figure 1d). For a triangular ice edge, the fetch field does not feature any discontinuities, but isolines in fetch over open water reflect the triangular geometry of the ice edge (Figure 1e). As in the control setup, the white wedges in the respective lower right corners in Figures 1d and 1e mark regions in which the flow cannot be traced back to the inflow boundary.

As the basic-state flow is geostrophically balanced, surface pressure p_s decreases considerably in crosswind direction. Prescribed temperatures are nearly constant in the cross-wind direction, such that density scales linearly with pressure. The varying surface pressure thus poses a challenge when comparing surface fluxes for the same fetch, because air density affects the magnitude of the air-sea exchange. The sensible heat flux

$$Q_{sens} = \frac{c_p \rho \kappa^2}{\psi_x^{(10)} \psi_T^{(2)}} U_{10} \left(\theta_{skin} - \theta_2 \right) \tag{2}$$

is determined by 10-m wind speed U_{10} and 2-m potential temperature θ_2 using the stability functions ψ_x and ψ_T for momentum and potential temperature, respectively, evaluated at the height in meters given in parenthesis. κ is the van-Karman constant, c_p the specific heat capacity of moist air at constant pressure, and ρ the air density at the lowest model level.

In summary, $Q_{\text{sens}} \propto \rho$ in Equation 2 and $\rho \propto p_s$. To be able to better compare the heat exchange across different cross-wind positions, we normalize both sensible and latent heat fluxes to a reference pressure of 1,000 hPa,

$$Q_{sens,norm} = \frac{1000\text{hPa}}{p_s} Q_{sens}, \tag{3}$$

and analogously for the latent heat flux. With this normalization, the variability in fluxes across different locations with the same fetch is minimized (shading around the curves in Figures 2a and 2b).

4. Control Simulation

Our control simulation is based on the control setup with a straight sea ice edge featuring a sharp transition from 100% sea-ice cover upstream to open ocean downstream of the sea ice edge. We use the simulation with 3 km grid spacing as our control simulation with a typical cold air outbreak evolution of the boundary layer (potential temperature, boundary layer height and clouds shown in Figure 1f).

The initially intense warming declines with increasing fetch (Figure 1f). In the boundary layer below the clouds, the isentropes are oriented nearly upright, indicating a well-mixed layer. First clouds form about 250 km downstream of the ice-edge. Except for a step around a fetch of 600 km, the cloud base is nearly horizontal throughout all fetches, suggesting an approximately constant offset between near-surface temperature and dew point.

Both the sensible and latent heat flux peak slightly downstream of the ice edge (Figures 2a and 2b). The respective maxima of about 400 W m^{-2} and 175 W m^{-2} are located at the fourth or fifth grid point of open water. This slight distance between the ice edge and the peak fluxes results from the fluxes depending on both the temperature and moisture contrasts as well as the wind speed. While the temperature and moisture contrasts decrease rapidly due to the fluxes, the wind speed increases from just below 12 m/s over sea ice to just below 16 m/s at a fetch of about 30 km (Figure 2e).

5. Sensitivity to Model Resolution

Both the magnitude and the position of the peak sensible heat flux off the ice edge are very consistent between simulations with a grid spacing between 3 km and 24 km (Figure 2a). At 3 km resolution, the strongest fluxes occur between 9 and 12 km off the ice edge, such that grid spacings up to 24 km capture this maximum well. Consistently, the peak sensible heat flux is noticeably lower only at 48 km and 96 km. Nevertheless, integrated over the first 96 km of fetch, more sensible heat is extracted in the 96 km simulation than in the 3 km simulation (red curve in Figure 2c). More generally, lower resolution simulations tend to extract more heat in the first 400 km off the ice edge, but less between a fetch of 400 and 700 km. At even larger fetches, slight but systematic differences appear between the simulations with most heat extracted at intermediate resolution (12 and 24 km grid spacing). Integrated up to 1,500 km, the total sensible heat extracted from the ocean varies only by about 1% between 3 and 96 km and is thus remarkably consistent across these resolutions.

The sensible heat fluxes in Figure 2a are determined by both near-surface temperature contrast and near-surface wind (Equation 2). Wind speeds are largely consistent across resolutions (Figure 2e), and differences in the sensible heat flux are mainly determined by differences in the near-surface temperature contrast (not shown).

In contrast to the sensible heat flux, the latent heat flux is not consistent across resolutions (Figure 2b). Latent heat fluxes consistently decrease with resolution at all fetches. Consequently, an increase in resolution yields a considerable increase in the total latent heat a simulated cold-air outbreak extracts from the ocean.

For precipitation, the dependence on resolution is even more pronounced (Figure 2e). A lower resolution results in a precipitation commencing closer to the ice edge. For example, at 96 km grid spacing a slight drizzle occurs already in the second grid cell off the ice edge, whereas precipitation commences at a fetch of about 300 km in the simulation with 3 km grid spacing.

In addition, the structure of precipitation also changes with resolution. At higher resolution, convection starts to organize into linear features with roll convection and cloud streets (cf. Chlond, 1992; Muller et al., 1999). For example, such linear features emerge in the moisture field at 300 m altitude in the 12 km-simulation in Figure 1c at a fetch of about 1,000 km, just upstream of a slight peak in precipitation (Figure 2e). At 6 and 3 km grid spacing, roll convection emerges closer to the ice edge (around 700 and 500 km fetch, respectively; not shown) and yields more pronounced downstream peaks in precipitation (Figure 2e).

The onset of roll convection is thus critically dependent on resolution, with higher resolution yielding earlier onsets. The peak in precipitation shifts considerably from 6 km to 3 km grid spacing, indicating that the model solution has not converged yet at our highest resolution.

At 1,500 km fetch the simulations point to two distinct precipitation regimes. The highest resolutions (3 km and 6 km grid spacing) equilibrated at a precipitation rate of approximately 2 mm/day, lower resolutions at about half that value (Figure 2e). The simulation with 12 km grid spacing does not recover to higher precipitation rates at higher fetches, although roll convection has set in (not shown). This grouping of simulations into precipitation regimes coincides with the grouping by enabled/disabled convection parametrization. This coincidence, however, is by chance. When running our highest resolution cases with convection parametrization enabled, our results do not change.

The different precipitation regimes have only a minor impact on the evaporation minus precipitation moisture budget of the atmosphere ($E - P$; Figure 2f). At large fetches, all simulations equilibrate at a net moistening of the atmosphere equivalent to about 2 mm of precipitable water per day. The higher rate of precipitation at higher resolution is thus largely offset by higher latent heat fluxes (Figure 2b), keeping the atmospheric moisture content approximately constant across resolutions, but invigorating the atmospheric water cycle.

In summary, both the integral sensible heat extraction and the moisture budget is remarkably consistent across resolutions. Nevertheless, there are systematic biases in lower resolution simulations that can affect atmosphere-ocean interactions (cf. Condron & Renfrew, 2013; Jung et al., 2014). For example, the latent heat flux increases with increasing resolution at all fetches. This increased moisture uptake is offset by increased precipitation, implying a more vigorous atmospheric water cycle at higher resolution. The more vigorous water cycle implies an increased heat transport from the ocean to the atmosphere because the latent heat of condensation is taken up from the ocean but released in the atmosphere.

6. Sensitivity to the Sharpness of the Marginal Ice Zone

The sensitivity to model resolution is likely more pronounced than presented above, as we designed the control setup such that the sea ice edge remains perfectly sharp at all model resolutions. For more realistic setups, the implicit smoothing when interpolating a given sea-ice concentration on a model grid likely exacerbates the effects. We therefore assess the sensitivity of the air-sea heat exchange to combinations of model resolution and the sharpness of the marginal ice zone (MIZ). In addition to the sharp ice edge in the control simulation, we evaluate transitions following a linear profile, ("L50" and "L200"), a tanh-shape ("T50" and "T200") defined by

$$SIC_T = \frac{1}{2} - \frac{1}{2}\tanh\frac{x - x_0}{L_x}, \tag{4}$$

as well as the convex and concave branches of the tanh-function ("TU50", "TU200", and "TL50", "TL200", respectively), defined by

$$SIC_{TU} = -\min\left(0, \tanh\frac{x - x_0}{L_x}\right), \tag{5}$$

$$SIC_{TL} = 1 - \max\left(0, \tanh\frac{x - x_0}{L_x}\right). \tag{6}$$

For each of the transitions, we tested the sharpness scales $L_x = 50$ km and $L_x = 200$ km, and x_0 is adjusted such that total sea-ice covered area remains constant across simulations. All profiles for $L_x = 50$ km are shown in Figure 3a.

Overall, a smoother transition from sea ice to open ocean yields lower peak sensible heat fluxes (Figure 3b). In the smoothest profile (T200), the peak flux is reduced by nearly 50% compared to the sharp sea ice edge. In comparison to the sensitivity to the smoothness of the MIZ, peak fluxes are largely consistent across

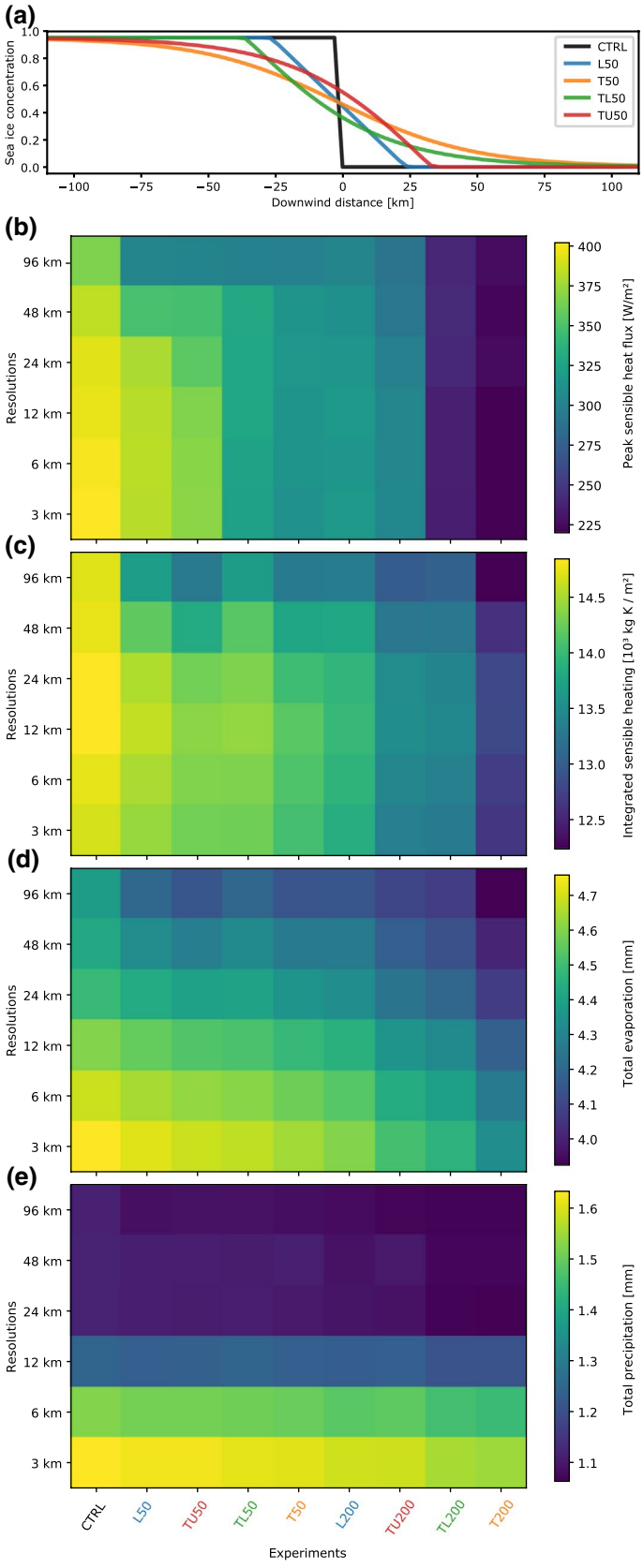
(a)
Sea ice concentration
Downwind distance [km]
CTRL
L50
T50
TL50
TU50
(b)
Peak sensible heat flux [W/m²]
(c)
Integrated sensible heating [10³ kg K / m²]
(d)
Total evaporation [mm]
(e)
Total precipitation [mm]
Resolutions
96 km
48 km
24 km
12 km
6 km
3 km
CTRL
L50
TU50
TL50
T50
L200
TU200
TL200
T200
Experiments

model resolutions, in particular for grid spacings between 3 km and 24 km. Only for the sharpest MIZs is the peak heat flux considerably reduced at the lowest resolutions (cf. 48 and 96 km for the L50 and TU50 simulations in Figure 3b).

For the peak fluxes, it matters where the sharpest gradient in sea-ice concentration occurs within the MIZ. The TL and TU-profiles are symmetric, but differ in whether the sharpest transition occurs either close to the open ocean (TU) or close to sea ice pack (TL). Here, the TL simulations yield markedly lower peak fluxes compared to the TU simulations at both 50 km and 200 km MIZ width scale (Figure 3b). Hence, it is mainly the sharpness of the MIZ at low sea ice concentrations that determines the peak heat flux.

Integral sensible heat uptake is even less dependent on model resolution than the peak sensible heat flux (Figures 3b and 3c). Consistent with the control simulations, integral fluxes for all MIZs are slightly higher at intermediate resolutions (12 km and 24 km grid spacing) compared to both higher and lower-resolution results (Figure 3c). This effect however is about one order of magnitude smaller than the reduction of integral heat uptake with smoother MIZs. The difference in integral heat uptake between the sharpest and the smoothest transitions amounts to about 20% (integrated up to a fetch of 1,500 km; Figure 3c). In contrast to the peak fluxes, the integral heat uptake is nearly identical for the TL and the TU simulations. The integral heat uptake is thus largely insensitive to where the sharpest gradient in ice concentration is located.

Overall, we find a clear dependence of the sensible heat uptake on the sharpness of the MIZ as well as on model resolution. Whereas in our control simulation the sea-ice edge remained perfectly sharp at all resolutions, not all tested transitions from sea ice to open ocean can be adequately resolved at all resolutions. The integral sensible heat uptake follows the resolved rather than prescribed sharpness of the MIZ, and is thus subject to resolution-dependent smoothing.

In the control simulations, we noted a marked effect of model resolution on the atmospheric water cycle, with both evaporation and precipitation decreasing as resolution is reduced. These results for reduced resolution translate only partially to a smoother MIZ. Whereas integral moisture uptake decreases with a smoother MIZ (Figure 3d), precipitation does not (Figure 3e). Consequently, a smoother MIZ leads to an overall dryer boundary layer, in particular at larger fetches.

These sensitivities have implications for the dynamics of CAOs in climate models, because the comparatively low atmospheric resolution will generally imply a smoothing of the represented MIZ. Our results therefore suggest that CAOs in climate models are biased toward an underrepresentation of air-sea exchange in CAOs, both regarding the peak and integral atmospheric heat uptake.

7. Sensitivity to the Geometry of the Marginal Ice Zone

In our sensitivity analysis on the sharpness of the MIZ, we kept the sea ice edge as a straight line, oriented perpendicular to the basic state wind. We now proceed to assess the sensitivity of the air-sea heat exchange to the geometry of the MIZ. Specifically, we compare the air-sea exchange for upwind and downwind steps in the sea ice edge as well as convex and concave triangles (Figure 4). In this analysis we compare grid cells with the same fetch across different simulations, irrespective of where they occur in the model domain. To isolate the effect of the geometry, we prescribe these shapes with a perfectly sharp sea ice edge. Many shapes nevertheless imply partly ice covered grid cells, yielding an implicit smoothing of the sea ice edge with decreasing resolution.

Overall, the geometry of the sea ice edge has only little impact on the peak sensible heat flux (Figure 4b). To first order, the fluxes depend only on the grid spacing, but not on the shape of the sea ice edge. The implicit smoothing when decreasing the resolution is particularly visible for the 96 km simulations, where the peak fluxes are reduced by 20%–25% compared to the CTRL simulation in which the sea-ice edge coincides with

Figure 3. Sensitivity of air-sea heat exchange on both the sharpness of the marginal ice zone and model grid spacing. (a) Profiles of sea ice concentration across the marginal ice zone with a width of 50 km. (b–d) Matrices of (b) peak sensible heat fluxes ($W m^{-2}$), (c) integrated sensible heating (10^3 kg K m^{-2}), (d) total evaporation (mm), and (e) total precipitation [mm], all integrated up until a fetch of 1,500 km. All matrices show the dependence on model grid spacing and the sea ice distribution within the marginal ice zone. The sea ice distribution in the experiments follows the profiles of (a) with width of 50 km and 200 km, respectively.

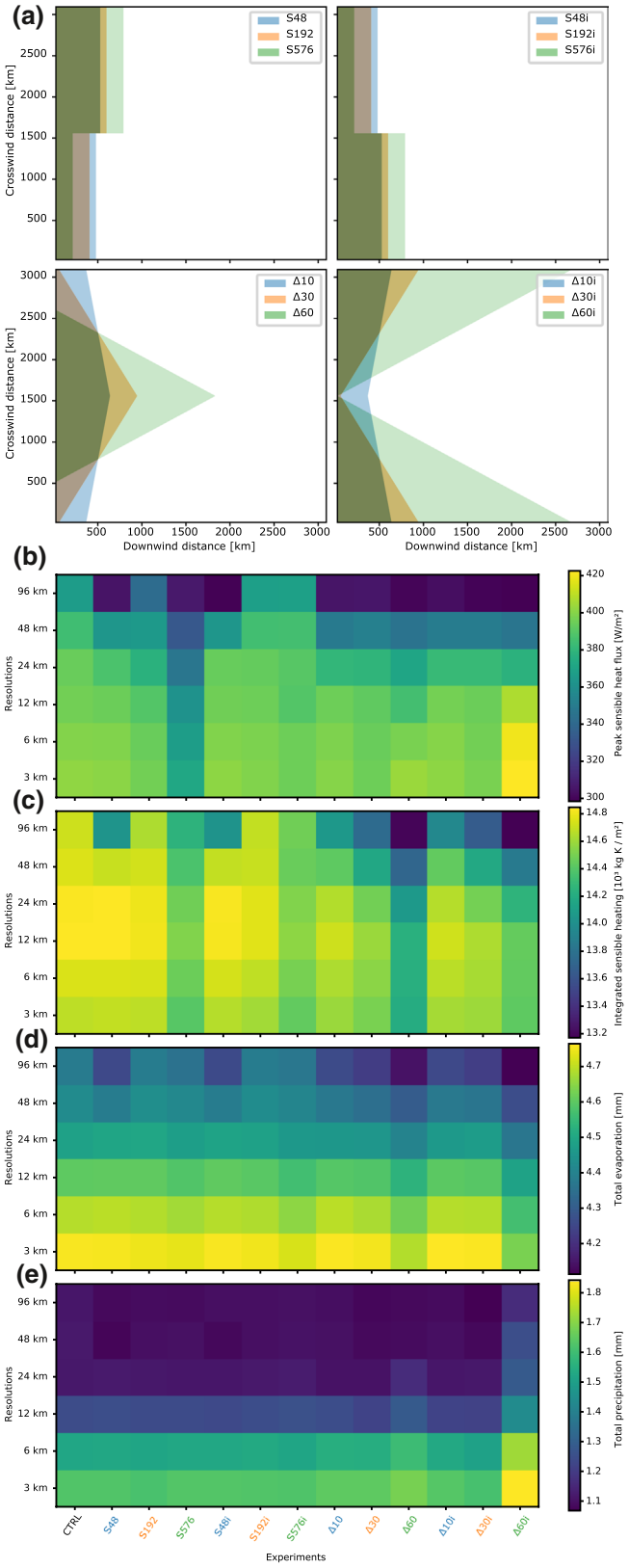

Figure 4. Sensitivity of air-sea heat exchange on both the shape of the marginal ice zone and model grid spacing. (a) Maps of sea ice cover for the different sensitivity experiments. (b–e) Matrices analogous to Figures 3b–3d, but showing the dependence on model grid spacing and the geometry of the sea ice edge.

a grid cell boundary (Figure 4b). Exceptions to this rule are the CTRL, S192, S192i, and S576i simulations, in which the sea ice edge remains perfectly sharp at all resolutions. Peak heat fluxes for the S576-simulation are nevertheless reduced at all resolutions, likely because of the slight on-ice flow along the step (cf. Discussion of Figure 1d in Section 3), which occurs at low fetch values and thus reduces the average heat flux at these fetches.

Similar to the peak heat fluxes, the integrated heat and moisture uptake is largely independent from the geometry of the sea ice edge. Exceptions occur for the narrowest triangles and largest up/downwind steps, featuring pronounced deviations from the straight sea ice edge. In these cases, the sea ice edge induces convergence or divergence lines and thus a degree of mesoscale flow organization. With this organization, the boundary layer evolution along neighboring stream lines is no longer independent. Any such flow organization tends to reduce the integral heat and moisture uptake (Figures 4c and 4d), although peak fluxes can also be amplified. For example, in the narrowest concave triangle (Δ60i), the peak sensible heat flux is about 5% stronger compared to the straight sea ice edge.

The atmospheric moisture is largely insensitive to the shape of the sea ice edge (Figures 4d and 4e). Only in the narrowest triangular shapes (Δ60, Δ60i), the moisture cycle is noticeably affected. Here, overall reduced moisture uptake and increased precipitation lead to an overall dryer atmosphere, especially for Δ60i, where the convergence zone appears to enhance precipitation efficiency.

In summary, air-sea heat exchange is remarkably consistent across all but the most pronounced deviations from a straight sea ice edge. Thus for most geometries, the distance traveled over open water largely determines the state of the atmospheric boundary layer. This implies that the boundary layer evolution along one stream line is largely independent from the evolution along other stream lines. This is plausible in the absence of mesoscale flow features such as convergence or divergence lines.

8. Summary and Conclusions

We used idealized simulations of a cold-air outbreak using the Polar WRF model to investigate the sensitivity of the air-sea heat exchange to model resolution, sharpness of the marginal ice zone (MIZ), and geometry of the sea ice edge. We characterized differences in the evolution of an atmospheric air column moving off the sea ice in terms of fetch, the distance traveled over open water. Based on these sensitivity analyses we draw the following conclusions:

1. The *resolved sharpness of the MIZ* strongly affects the peak magnitude of air-sea heat exchange. In particular, peak fluxes are sensitive to the sharpness of the MIZ close to the open ocean. An abrupt end of the MIZ toward the open ocean leads to comparatively higher fluxes.
2. *Model resolution* strongly affects the atmospheric water cycle. The higher the model resolution, the smaller the minimum horizontal scale of resolved roll convection and the smaller the fetch at which roll convection occurs in the simulations. Such roll convection simultaneously increases evaporation and precipitation, leaving the net atmospheric moisture budget more or less unchanged across experiments while increasing the atmospheric latent heat uptake. There is no indication that the atmospheric water cycle has converged at our highest resolution with 3 km grid spacing.
3. The *geometry of the sea ice edge* only affects peak and integral heat fluxes when it induces pronounced convergence or divergence zones within the cold air outbreak. Such internal flow asymmetries generally decrease the total heat and moisture uptake within the cold air outbreak, but at the same time generally increase precipitation. Mesoscale flow organization in a cold air outbreak thus results in a dryer boundary layer.
4. A state *without mesoscale flow organization* and a perfectly sharp MIZ seems to be the *optimal setup for extracting heat from the ocean*. In our sensitivity analysis, any deviation from such a state, by smoothing the MIZ or inducing crosswind asymmetries, decreases the overall heat and moisture uptake. At the same time, precipitation remains either about constant (smoothing of the MIZ) or might even increase (triangular edge geometries), leading to an overall dryer atmosphere.

The outlined sensitivities have significant implications for the ocean underlying a modeled cold air outbreak. Higher atmospheric resolution increases both the peak heat fluxes as well as the integral heat transfer from the ocean to the atmosphere. In a coupled system, this would result in a more locally confined

destabilization of the oceanic water column as well as a stronger cooling of the ocean also downstream. Furthermore, the sensitivity to the sea ice concentration in the MIZ suggests that both the resolved sharpness of the MIZ and the internal sea ice dynamics determining the sea ice distribution are key to adequately represent the air-sea heat exchange within and downstream of the MIZ.

Data Availability Statement

The WRF Model (WRF Maintainers, 2017), the Polar WRF modifications (Available after registration; Polar Meteorology Group of Byrd Polar Research Center, 2017), and the code to produce the WRF initial conditions (InitJET Contributors, 2019) are all publicly available.

Acknowledgments
The authors thank Annick Terpstra for interesting discussions and providing the basis of the code used to create the WRF initial state and boundary forcing. The authors thank the National Center for Atmospheric Research (NCAR) for developing and making available the WRF model and the Polar Meteorology group at the Ohio State University for providing the Polar WRF modifications. The authors acknowledge internal funding within the Bjerknes Center for Climate Research to the Atmosphere-Ocean-Ice interaction project (AOI) and the computing resources provided by UNINETT Sigma2 AS through projects NN9624K and NN9625K.

References

Bourassa, M. A., Gille, S. T., Bitz, C., Carlson, D., Cerovecki, I., Clayson, C. A., et al. (2013). High-latitude ocean and sea ice surface fluxes: Challenges for climate research. *Bulletin of the American Meteorological Society*, *94*(3), 403–423. https://doi.org/10.1175/BAMS-D-11-00244.1

Brummer, B. (1996). Boundary-layer modification in wintertime cold-air outbreaks from the Arctic sea ice. *Boundary-Layer Meteorology*, *80*(1), 109–125. https://doi.org/10.1007/BF00119014

Brummer, B. (1997). Boundary layer mass, water, and heat budgets in wintertime cold-air outbreaks from the Arctic sea ice. *Monthly Weather Review*, *125*(8), 1824–1837. https://doi.org/10.1175/1520-0493(1997)125(1824:BLMWAH)©2.0.CO;2

Chen, S.-H., & Sun, W.-Y. (2002). A one-dimensional time dependent cloud model. *Journal of the Meteorological Society of Japan. Ser. II*, *80*(1), 99–118. https://doi.org/10.2151/jmsj.80.99

Chlond, A. (1992). Three-dimensional simulation of cloud street development during a cold air outbreak. *Boundary-Layer Meteorology*, *58*(1), 161–200. https://doi.org/10.1007/BF00120757

Condron, A., Bigg, G. R., & Renfrew, I. A. (2008). Modeling the impact of polar mesocyclones on ocean circulation. *Journal of Geophysical Research: Oceans*, *113*(C10). https://doi.org/10.1029/2007JC004599

Condron, A., & Renfrew, I. A. (2013). The impact of polar mesoscale storms on northeast Atlantic Ocean circulation. *Nature Geoscience*, *6*(1), 34–37. https://doi.org/10.1038/ngeo1661

Dickson, R., Lazier, J., Meincke, J., & Rhines, P. (1996). Long-term coordinated changes in the convective activity of the North Atlantic. In D. L. T. Anderson & J. Willebrand (Eds.), *Decadal climate variability* (pp. 211–261). Berlin, Heidelberg: Springer Berlin Heidelberg.

Gebbie, G., & Huybers, P. (2010). Total matrix intercomparison: A method for determining the geometry of water-mass pathways. *Journal of Physical Oceanography*, *40*(8), 1710–1728. https://doi.org/10.1175/2010JPO4272.1

Haarsma, R. J., Roberts, M. J., Vidale, P. L., Senior, C. A., Bellucci, A., Bao, Q., et al. (2016). High resolution model intercomparison project (highresmip v1.0) for cmip6. *Geoscientific Model Development*, *9*(11), 4185–4208. https://doi.org/10.5194/gmd-9-4185-2016

Hines, K. M., Bromwich, D. H., Bai, L., Bitz, C. M., Powers, J. G., & Manning, K. W. (2015). Sea ice enhancements to Polar WRF. *Monthly Weather Review*, *143*(6), 2363–2385. https://doi.org/10.1175/MWR-D-14-00344.1

Hong, S.-Y., Noh, Y., & Dudhia, J. (2006). A new vertical diffusion package with an explicit treatment of entrainment processes. *Monthly Weather Review*, *134*(9), 2318–2341. https://doi.org/10.1175/MWR3199.1

InitJET Contributors. (2019). initjet repository on github. Retrieved 22 January 2021, from https://github.com/aterpstra/initjet

Inoue, J., & Hori, M. E. (2011). Arctic cyclogenesis at the marginal ice zone: A contributory mechanism for the temperature amplification? *Geophysical Research Letters*, *38*(12). https://doi.org/10.1029/2011gl047696

Isachsen, P. E., Drivdal, M., Eastwood, S., Gusdal, Y., Noer, G., & Saetra, O. (2013). Observations of the ocean response to cold air outbreaks and polar lows over the Nordic Seas. *Geophysical Research Letters*, *40*(14), 3667–3671. https://doi.org/10.1002/grl.50705

Jung, T., Serrar, S., & Wang, Q. (2014). The oceanic response to mesoscale atmospheric forcing. *Geophysical Research Letters*, *41*(4), 1255–1260. https://doi.org/10.1002/2013GL059040

Kain, J. S. (2004). The Kain-Fritsch convective parameterization: An update. *Journal of Applied Meteorology*, *43*(1), 170–181. https://doi.org/10.1175/1520-0450(2004)043(0170:TKCPAU)©2.0.CO;2

Manning, K. (2019). *Current AMPS configuration*. Retrieved 22 January 2021, from https://www2.mmm.ucar.edu/rt/amps/information/configuration/configuration.html

Michel, C., Terpstra, A., & Spengler, T. (2018). Polar mesoscale cyclone climatology for the Nordic seas based on era-interim. *Journal of Climate*, *31*(6), 2511–2532. https://doi.org/10.1175/JCLI-D-16-0890.1

Moore, G. W. K., Bromwich, D. H., Wilson, A. B., Renfrew, I., & Bai, L. (2016). Arctic system reanalysis improvements in topographically forced winds near Greenland. *Quarterly Journal of the Royal Meteorological Society*, *142*(698), 2033–2045. https://doi.org/10.1002/qj.2798

Muller, G., Brummer, B., & Alpers, W. (1999). Roll convection within an Arctic cold-air outbreak: Interpretation of in situ aircraft measurements and spaceborne SAR imagery by a three-dimensional atmospheric model. *Monthly Weather Review*, *127*(3), 363–380. https://doi.org/10.1175/1520-0493(1999)127(0363:RCWAAC)©2.0.CO;2

Nakanishi, M., & Niino, H. (2006). An improved mellor–yamada level-3 model: Its numerical stability and application to a regional prediction of advection fog. *Boundary-Layer Meteorology*, *119*(2), 397–407. https://doi.org/10.1007/s10546-005-9030-8

Nakanishi, M., & Niino, H. (2009). Development of an improved turbulence closure model for the atmospheric boundary layer. *Journal of the Meteorological Society of Japan. Ser. II*, *87*(5), 895–912. https://doi.org/10.2151/jmsj.87.895

Papritz, L., & Spengler, T. (2017, January). A lagrangian climatology of wintertime cold air outbreaks in the Irminger and Nordic seas and their role in shaping air-sea heat fluxes. *Journal of Climate*, *30*(8), 2717–2737.Retrieved from https://doi.org/10.1175/JCLI-D-16-0605.1

Pickart, R. S., Spall, M. A., Ribergaard, M. H., Moore, G. W. K., & Milliff, R. F. (2003). Deep convection in the Irminger sea forced by the Greenland tip jet. *Nature*, *424*(6945), 152–156. https://doi.org/10.1038/nature01729

Polar Meteorology Group of Byrd Polar Research Center. (2017). Polar wrf. Retrieved 22 January 2021, from http://polarmet.osu.edu/PWRF/

Renfrew, I. A., Barrell, C., Elvidge, A. D., Brooke, J. K., Duscha, C., King, J. C., et al. (2021). An evaluation of surface meteorology and fluxes over the Iceland and Greenland Seas in ERA5 reanalysis: The impact of sea ice distribution. *Quarterly Journal of the Royal Meteorological Society*, *147*(734), 691–712. https://doi.org/10.1002/qj.3941

Renfrew, I. A., & King, J. C. (2000). A simple model of the convective internal boundary layer and its application to surface heat flux estimates within polynyas. *Boundary-Layer Meteorology*, *94*(3), 335–356. https://doi.org/10.1023/A:1002492412097

Renfrew, I. A., Pickart, R. S., Vage, K., Moore, G. W. K., Bracegirdle, T. J., Elvidge, A. D., et al. (2019). The Iceland Greenland seas project. *Bulletin of the American Meteorological Society*, *100*(9), 1795–1817. https://doi.org/10.1175/BAMS-D-18-0217.1

Sein, D. V., Koldunov, N. V., Danilov, S., Sidorenko, D., Wekerle, C., Cabos, W., et al. (2018). The relative influence of atmospheric and oceanic model resolution on the circulation of the north Atlantic ocean in a coupled climate model. *Journal of Advances in Modeling Earth Systems*, *10*(8), 2026–2041. https://doi.org/10.1029/2018MS001327

Seo, H., & Yang, J. (2013). Dynamical response of the Arctic atmospheric boundary layer process to uncertainties in sea-ice concentration. *Journal of Geophysical Research: Atmospheres*, *118*(22), 12383–12402. https://doi.org/10.1002/2013JD020312

Spengler, T., Renfrew, I. A., Terpstra, A., Tjernstrom, M., Screen, J., Brooks, I. M., et al. (2016). High-latitude dynamics of atmosphere–ice–ocean interactions. *Bulletin of the American Meteorological Society*, *97*(9), ES179–ES182. https://doi.org/10.1175/BAMS-D-15-00302.1

Stoll, P. J., Graversen, R. G., Noer, G., & Hodges, K. (2018). An objective global climatology of polar lows based on reanalysis data. *Quarterly Journal of the Royal Meteorological Society*, *144*(716), 2099–2117. https://doi.org/10.1002/qj.3309

Stoll, P. J., Spengler, T., Terpstra, A., & Graversen, R. G. (2021). Polar lows – moist-baroclinic cyclones developing in four different vertical wind shear environments. *Weather and Climate Dynamics*, *2*(1), 19–36. https://doi.org/10.5194/wcd-2-19-2021

Strong, C. (2012). Atmospheric influence on Arctic marginal ice zone position and width in the Atlantic sector, February–April 1979–2010. *Climate Dynamics*, *39*(12), 3091–3102. https://doi.org/10.1007/s00382-012-1356-6

Sukoriansky, S., Galperin, B., & Perov, V. (2005). Application of a new spectral theory of stably stratified turbulence to the atmospheric boundary layer over sea ice. *Boundary-Layer Meteorology*, *117*(2), 231–257. https://doi.org/10.1007/s10546-004-6848-4

Terpstra, A., Michel, C., & Spengler, T. (2016). Forward and reverse shear environments during polar low genesis over the northeast Atlantic. *Monthly Weather Review*, *144*(4), 1341–1354. https://doi.org/10.1175/MWR-D-15-0314.1

Terpstra, A, & Spengler, T (2015). An Initialization Method for Idealized Channel Simulations. *Monthly Weather Review*, *143*(6), 2043–2051.

Vage, K., Papritz, L., Havik, L., Spall, M. A., & Moore, G. W. K. (2018). Ocean convection linked to the recent ice edge retreat along east Greenland. *Nature Communications*, *9*(1), 1287. https://doi.org/10.1038/s41467-018-03468-6

Vage, K., Pickart, R. S., Moore, G. W. K., & Ribergaard, M. H. (2008). Winter mixed layer development in the central Irminger Sea: The effect of strong, intermittent wind events. *Journal of Physical Oceanography*, *38*(3), 541–565. https://doi.org/10.1175/2007JPO3678.1

WRF Maintainers. (2017). WRF releases on github. Retrieved 22 January 2021, from https://github.com/wrf-model/WRF/releases